A Homogenized Energy Model for the Direct Magnetomechanical Effect

Ralph C. Smith
Center for Research in Scientific Computation
Department of Mathematics
North Carolina State University
Raleigh, NC 27695-8205
rsmith@eos.ncsu.edu

Marcelo J. Dapino
Department of Mechanical Engineering
The Ohio State University
Columbus, OH 43210
dapino.1@osu.edu

Abstract

This paper focuses on the development of a homogenized energy model which quantifies certain facets of the direct magnetomechanical effect. In the first step of the development, Gibbs energy analysis at the lattice level is combined with Boltzmann principles to quantify the local average magnetization as a function of input fields and stresses. A macroscopic magnetization model, which incorporates the effects of polycrystallinity, material nonhomogeneities, stress-dependent interaction fields, and stress-dependent coercive behavior, is constructed through stochastic homogenization techniques based on the tenet that local coercive and interaction fields are manifestations of underlying distributions rather than constants. The resulting framework incorporates previous ferromagnetic hysteresis theory as a special case in the absence of applied stresses. Attributes of the framework are illustrated through comparison with previously published steel and iron data.

Report Documentation Page		*Form Approved* *OMB No. 0704-0188*

Public reporting burden for the collection of information is estimated to average 1 hour per response, including the time for reviewing instructions, searching existing data sources, gathering and maintaining the data needed, and completing and reviewing the collection of information. Send comments regarding this burden estimate or any other aspect of this collection of information, including suggestions for reducing this burden, to Washington Headquarters Services, Directorate for Information Operations and Reports, 1215 Jefferson Davis Highway, Suite 1204, Arlington VA 22202-4302. Respondents should be aware that notwithstanding any other provision of law, no person shall be subject to a penalty for failing to comply with a collection of information if it does not display a currently valid OMB control number.

1. REPORT DATE **2005**	2. REPORT TYPE	3. DATES COVERED **-**

4. TITLE AND SUBTITLE **A Homogenized Energy Model for the Direct Magnetomechanical Effect**	5a. CONTRACT NUMBER
	5b. GRANT NUMBER
	5c. PROGRAM ELEMENT NUMBER
6. AUTHOR(S)	5d. PROJECT NUMBER
	5e. TASK NUMBER
	5f. WORK UNIT NUMBER
7. PERFORMING ORGANIZATION NAME(S) AND ADDRESS(ES) **Air Force Office of Scientific Research,875 North Randolph Street,Arlington,VA,22203-1768**	8. PERFORMING ORGANIZATION REPORT NUMBER
9. SPONSORING/MONITORING AGENCY NAME(S) AND ADDRESS(ES)	10. SPONSOR/MONITOR'S ACRONYM(S)
	11. SPONSOR/MONITOR'S REPORT NUMBER(S)

12. DISTRIBUTION/AVAILABILITY STATEMENT **Approved for public release; distribution unlimited**

13. SUPPLEMENTARY NOTES

14. ABSTRACT **see report**

15. SUBJECT TERMS

16. SECURITY CLASSIFICATION OF:			17. LIMITATION OF ABSTRACT	18. NUMBER OF PAGES	19a. NAME OF RESPONSIBLE PERSON
a. REPORT **unclassified**	b. ABSTRACT **unclassified**	c. THIS PAGE **unclassified**		**23**	

1 Introduction

The characterization of magnetoelastic effects is a classical problem which has significant ramifications for both material characterization and magnetic transducer design. The generation of strains due to field-induced moment rotation or domain wall movement is fundamental for actuator design whereas characterization of magnetization changes due to input stresses is crucial for magnetic sensors as well as actuators operating in high stress regimes [12–14, 22]. The coupling between the two effects adds to the complexity of the phenomena.

In this paper, we focus on the characterization of the direct magnetomechanical effect, or Villari effect, which constitutes changes in the magnetization due to stress-induced domain wall movement and moment rotation. At the macroscopic level, this effect is delineated by a number of cooperative phenomena including (i) stress-dependent behavior of the anhysteretic magnetization M_{an}, anhysteretic induction B_{an}, remanent magnetization M_R, remanent induction B_R, and coercive field H_c, (ii) asymmetric magnetization response to compressive and tensile stresses, and (iii) decay of the magnetization M to M_{an} (equivalently B to B_{an}).

1.1 Stress-Dependence of M_{an}, B_{an}, M_R, B_R and H_c

The effect of stress on the anhysteretic and hysteretic behavior of steel are illustrated in Figure 1 with data from Pitman [21]. Similar behavior is reported in Bozorth [4] for 68 permalloy and nickel and Calkins [8] for Terfenol-D. It is observed that as stresses are changed from +100 MPa to −400 MPa, B_{an} transitions from almost constant behavior at $\pm B_s$ to a highly mollified curve with decreased
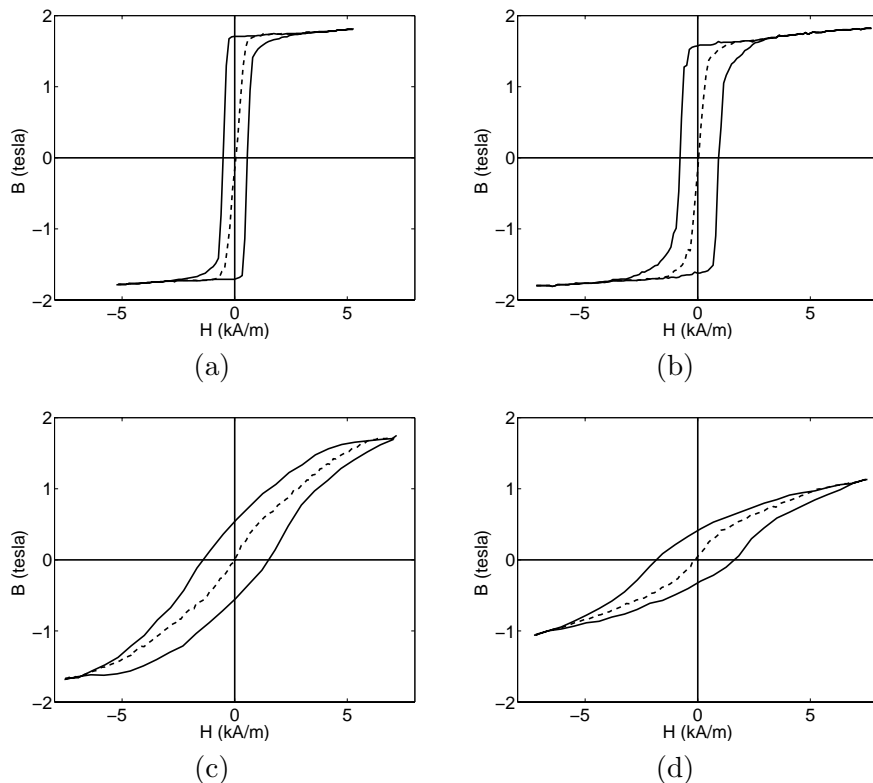

Figure 1: Hysteretic (——) and anhysteretic (– – –) H-B behavior of steel data from Pitman [21] for differing input stress levels: (a) 100 MPa, (b) 0 MPa, (c) -200 MPa, and (d) -400 MPa.

maximal values. For the hysteresis curves, the differential permeability $\frac{dB}{dH}$ is nearly constant for $\sigma = 100$ MPa which indicates a small degree of pre-remanence switching and yields a large remanence induction B_R. Conversely, there is significant pre-remanence switching for $\sigma = -400$ MPa which increases the coercive field H_c and significantly diminishes B_R.

The hysteresis data in Figure 1 illustrates one effect of stresses on the local interaction field H_I. The data collected with $\sigma = 100$ MPa exhibits negligible H_I and little pre-remanence switching. For large compressive stresses, however, H_I is sufficiently large that effective fields $H_e = H + H_I$ produce switching far in advance of remanence. As detailed by Goodenough [16], the decrease in H_I for tensile stresses can be attributed in part to stress-enhanced common easy axes between grains. The ramifications of these observations for model development will be discussed in Section 3.3.

The data obtained with fixed compressive stresses also illustrates that both the local coercive fields H_c and local interaction fields H_I are manifestations of underlying distributions rather than constant coefficients. The distributed nature of H_c is reflected in the observation that $\frac{dB}{dH}$ is finite at $\pm H_c$ whereas the variance in H_I is indicated by the fact $\frac{dB}{dH}$ is changing as the applied field is reduced to zero — materials having a small variance in H_I would exhibit nearly linear behavior differential permeabilities at remanence. The incorporation of densities for H_I and H_c to accommodate the effects of polycrystallinity, material nonhomogeneities, and various stress-dependencies is one of the hallmarks of the framework.

To further illustrate the anhysteretic behavior of steel, we plot in Figure 2 anhysteretic data from Jiles and Atherton [18] collected at higher field inputs than the Pitman steel data shown in Figure 1. The crossing of the anhysteretic curves at different field and stress values constitutes the Villari reversal and plays a fundamental role in the determination of appropriate Gibbs energy functionals. Additionally, it has been observed in [1, 23] that for biased operating regimes, the magnetization or induction can approach offset anhysteretic curves associated with biased minor loops. Hence theory must also accommodate this effect since transducers typically operate in such biased regimes.

The physical mechanisms which produce these macroscopic effects are complex and, for many materials and operating conditions, are not well understood. We summarize here only certain mechanisms which are pertinent for subsequent model development.

From a theoretical perspective, the anhysteretic magnetization (or induction) represents the *global* equilibrium configuration of the magnetization (or induction) for a specified field level. The pinning sites and easy axes provide *local* minima in underlying energy relations which determine the
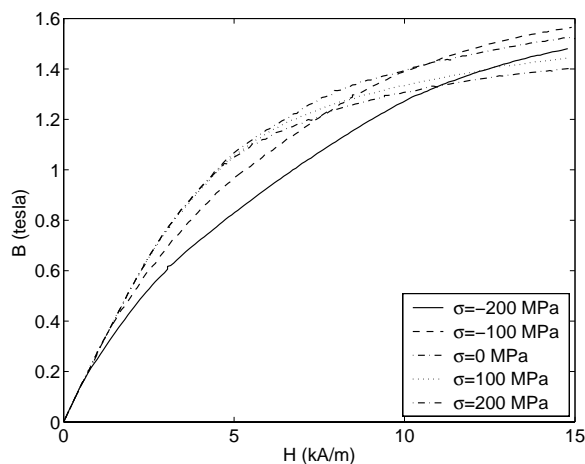

Figure 2: Stress-dependent anhysteretic data from Jiles and Atherton [18].

magnetization (or induction) unless sufficient energy is provided to overcome the local barriers and achieve the global minimum provided by M_{an} (B_{an}).

In the models developed in this paper, M_{an} depends on the choices of Gibbs energy and interaction field behavior. The stress-dependence and Villari reversal illustrated by the data in Figures 1 and 2 are accommodated through the choice of Gibbs functional and interaction field density.

1.2 Asymmetry of Magnetization (Induction) Changes for Tensile and Compressive Stresses

Asymmetry properties of the magnetomechanical effect for compressive and tensile stresses are illustrated in Figure 3 with steel data from Craik and Wood [10] collected at fixed field levels of 26.6 A/m and 132 A/m. For the first case, it is observed that for low stress levels (e.g., less than 10 MPa), positive and negative stress inputs produce similar changes in B. This forms the basis for Brown's theory [7] which posits that at low levels, positive and negative stresses have the same influence on 90° domain walls and hence produce equal changes in the magnetization or induction. However, some asymmetry between positive and negative stresses is observed at essentially all input levels and the asymmetry is profound at higher stress levels.

Additional observations which prove important for model development are the following.

(i) For $H = 26.6$ A/m, $\frac{dB}{d\sigma}$ changes sign at approximately $\sigma = 80$ MPa and $\sigma = -50$ MPa. This represents the tensile and stress levels required to drive B to the anhysteretic curve B_{an} at this fixed field level — see Section 3.1 for additional details regarding this phenomenon.

(ii) The slope $\frac{dB}{d\sigma}$ is discontinuous at the minimum value.

It will be demonstrated in Section 4 that similar properties are shared by data from other compounds.

In concert, these properties demonstrate that stress-induced pressure on 90° domain walls does not provide the sole mechanism producing magnetomechanical effects and additional mechanisms which must be incorporated include stress-induced changes in the anhysteretic magnetization (induction), stress-dependence of local coercive fields H_c, and anisotropic phenomena associated with preferential alignment with easy axes that coincide with applied stresses.

1.3 Approach to the Anhysteretic Curve

Figure 4 further illustrates the manner through which the application of an applied compressive stress drives the induction (equivalently, magnetization) near positive and negative remanence ($H =$
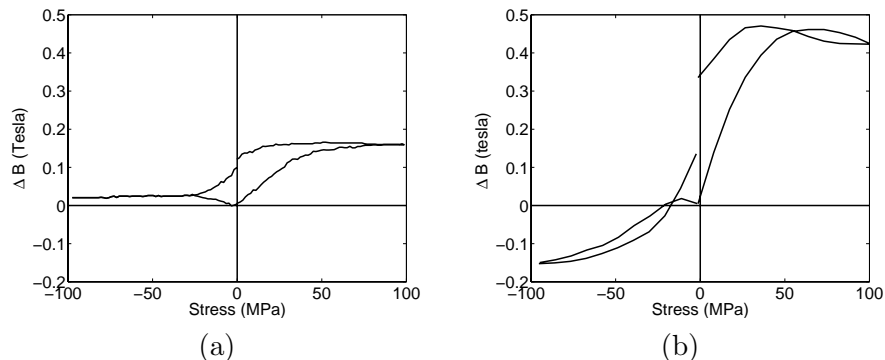

Figure 3: σ-B behavior of steel data from Craik and Wood [10] at field levels of (a) 26.6 A/m and (b) 132 A/m.
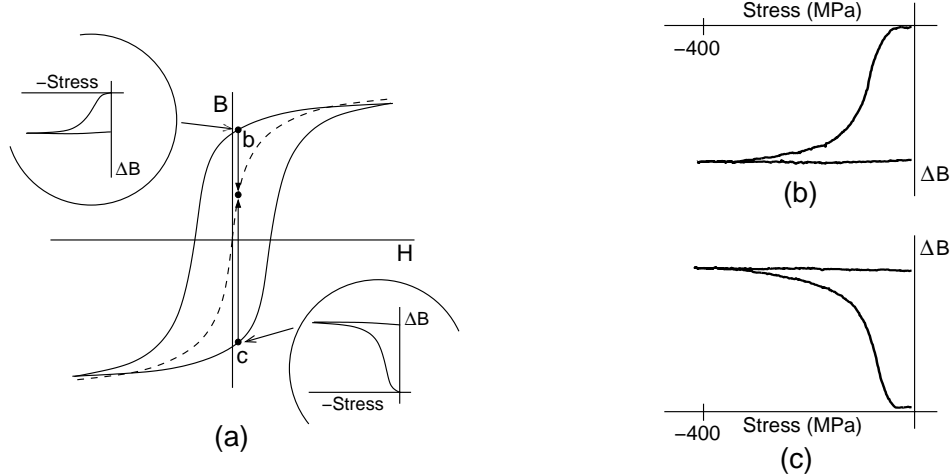
Figure 4: (a) Manner through which the magnetization near positive remanence is driven to the anhysteretic curve through application of compressive stresses; (b) and (c) steel data from Pitman [21] quantifying the σ-B behavior for steel near positive and negative remanence.

80 A/m) to the anhysteretic value B_{an} (M_{an}). As detailed in Pitman [21], a steel specimen was driven to both positive and negative saturation and then held at the constant field value 80 A/m while compressive stresses were applied and subsequently released. A comparison of the data plotted in Figures 4(b) and (c) illustrates that in both cases, the induction was driven to B_{an} by input stresses of approximately $\sigma = -300$ MPa. These stresses are thus sufficiently large to eliminate local minima associated with pinning sites so that the induction equilibrates to the global minimum associated with B_{an}. In other words, local coercive fields have been reduced to zero. Close examination of the σ-B relations upon stress release reveals that they are not constant thus reiterating the observation that the global minima associated with B_{an} are stress-dependent as illustrated in Figures 1 and 2.

Additionally, it has been observed that the rate and manner in which the induction or magnetization approaches the anhysteretic are also dependent on the stress rate $\frac{d\sigma}{dt}$. This rate-dependence was likely first noted by Ewing who observed that the remanence values and hysteresis associated with a soft iron wire were significantly reduced by a series of impacts [5, 23] whereas Brown [7] noted that for certain materials, a single impact was sufficient to drive M to M_{an}. Hence when modeling this phenomenon, we quantify the dependence of local coercive fields H_c on both σ and $\frac{d\sigma}{dt}$.

The stress-induced reduction in local coercive fields can be attributed in part to non-180° switching (90° domain wall movement in iron and steel). As noted previously, however, sole consideration of 90° domain wall movement does not explain the asymmetric changes shown in Figure 3 for compressive and tensile stresses. Hence 90° domain wall processes motivate aspects of the characterization framework but do not constitute the sole mechanism in the model.

1.4 Model Development

An early model for the direct magnetomechanical effect was provided by Brown [7] based on the tenet that at low levels, stress-induced changes in the magnetization obey Rayleigh's law. Whereas this theory predicts phenomena such as shock-induced magnetization changes, it does not accommodate the asymmetric tensile-compressive behavior shown in Figure 3. In [17, 20], Jiles and Li provide a model which does accommodate a number of the phenomena illustrated in Figures 1–4. This model extends the framework of Jiles and Atherton [18, 19] — which is based on the construction of anhysteretic, irreversible and reversible magnetization components M_{an}, M_{rev}, M_{irr} — through the

4

incorporation of stress-dependence in M_{an} and a law of approach based on the elastic energy. For feedback control applications, however, this framework can have limited utility since biased minor loop closure can only be enforced with *a priori* knowledge of turning points — with feedback control, turning points are dictated by state behavior which is typically unknown when control is initiated.

In this paper, we construct a model for the direct magnetomechanical effect with the goal of providing sufficient accuracy for material characterization and sufficient efficiency for optimal device design and real-time control implementation. To accommodate a wide range of magnetic actuator and sensor applications, the framework is constructed to encompass a broad range of inputs, operating conditions, and constituent materials, and to provide the robustness required for control design.

The model is based on the framework developed in [24–26] to quantify the hysteretic and nonlinear H-M and H-B behavior of ferromagnetic materials. In the first step of that development, Helmholtz and Gibbs energy relations are constructed at the lattice level to quantify the local average magnetization for homogeneous materials and effective fields. In the second step of the development, the effects of polycrystallinity, material nonhomogeneities, and variable effective fields are incorporated by positing that local coercive fields H_c and interaction fields H_I are manifestations of underlying distributions rather than constants. Stochastic homogenization in this manner provides macroscopic models which accurately characterize a wide range of material behavior — including closure of biased minor loops when appropriate, magnetic after-effects and thermal relaxation, and anhysteretic behavior — and are sufficiently efficient to permit subsequent control implementation.

Here we extend that framework to accommodate the stress-dependent magnetization behavior associated with the direct magnetomechanical effect. In the lattice-level energy relations, this requires extension of the Helmholtz and Gibbs energy expressions to incorporate elastic and magnetoelastic energy components associated with measured σ-M, σ-B, σ-M_{an} and σ-B_{an} behavior. In the stochastic homogenization component, we determine phenomenological expressions for the densities ν_1 and ν_2, associated with the local coercive field H_c and interaction field H_I, which accommodate the decay in coercivity observed in Figure 4 and changing interaction field behavior shown in the hysteresis data in Figure 1.

In [24], it is demonstrated that the original framework provides constitutive relations which can subsequently be used to construct distributed models for a wide range of actuators with field inputs. Similarly, the extended magnetomechanical model can be used to construct distributed models for magnetic sensors and actuators subjected to field and/or stress inputs.

In Section 2, we summarize the hysteresis framework of [24–26], and in Section 3, we extend it to construct the magnetomechanical model. Attributes of the model are demonstrated in Section 4 through fits to experimental steel and iron data.

2   Magnetic Hysteresis Model

To provide the underlying framework for the magnetomechanical model, we summarize first the model developed in [24–26] which quantifies the hysteresis and constitutive nonlinearities inherent to the H-M and H-B behavior of ferromagnetic materials. The model was developed in the context of uniaxial materials but is generally applicable to isotropic and weakly anisotropic materials. The framework provides the capability for incorporating magnetic after-effects and thermal relaxation but does not include eddy current losses; hence it should be employed for low frequency regimes or transducer architectures for which eddy current losses are minimal.

As detailed in [24–26], application of mean field theory at the lattice level yields the Helmholtz

energy relation

$$\psi(M,T) = \frac{H_h M_s}{2}\left[1 - (M/M_s)^2\right] + \frac{H_h T}{2T_c}\left[M\ln\left(\frac{M + M_s}{M_s - M}\right) + M_s\ln(1 - (M/M_s)^2)\right] \tag{1}$$

which quantifies the internal energy at temperature T. Here T_s, H_h and M_s respectively denote the Curie point for the material, a bias field, and the saturation magnetization. We note that (1) yields a double well potential for $T < T_c$ and a single well for $T > T_c$ so that T_c delineates the transition between ferromagnetic and paramagnetic phases.

For fixed temperature regimes, the efficiency and robustness of subsequent models can be improved by truncating Taylor expansions of (1) about the stable and unstable equilibria to obtain the piecewise quadratic relation

$$\psi(M) = \begin{cases} \frac{1}{2}\eta(M + M_R)^2 & , \ M \leq -M_I \\ \frac{1}{2}\eta(M - M_R)^2 & , \ M \geq M_I \\ \frac{1}{2}\eta(M_I - M_R)\left(\frac{M^2}{M_I} - M_R\right) & , \ |M| < M_I \end{cases}$$
$$= \begin{cases} \frac{1}{2}\eta(M - \delta M_R)^2 & , \ M \leq -M_I \\ \frac{1}{2}\eta(M + \delta M_R)^2 & , \ M \geq M_I \\ \frac{1}{2}\eta(M_I - M_R)\left(\frac{M^2}{M_I} - M_R\right) & , \ |M| < M_I \end{cases} \tag{2}$$

where $\delta = \text{sign}(M)$. As shown in Figure 5, the local remanence value M_R occurs at the positive $\text{argmin}(\psi)$, M_I is the positive inflection point, and η is the reciprocal of the slope for the hysteresis kernel after switching. For simplicity, we will focus on (2) throughout the remainder of the discussion while noting that analogous theory holds for (1) as detailed in [24–26].

The Gibbs energy relation

$$G(H, M) = \psi(M) - \mu_0 H M \tag{3}$$

incorporates the magnetostatic energy $\mu_0 H M$ which quantifies work due to an applied field (μ_0 denotes the permeability). The behavior of G for $H = 0$ and $H > 0$ is depicted in Figure 5(a).
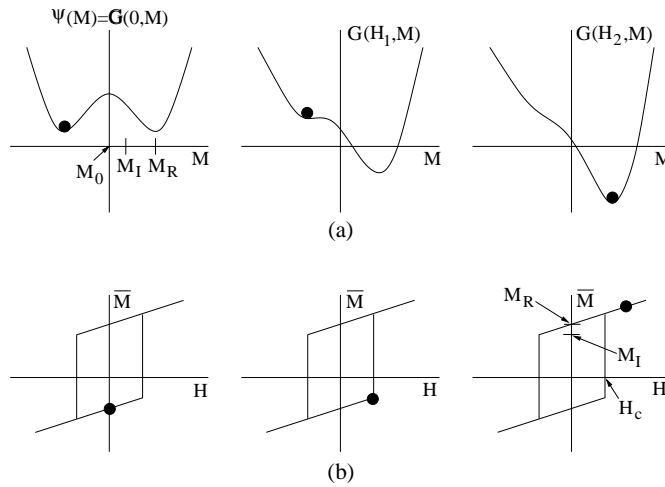

Figure 5: (a) Helmholtz energy ψ and Gibbs energy G for increasing field H ($H_2 > H_1 > 0$). (b) Dependence of the local average magnetization $\overline{M}$ given by (4) or (5) on the field in the absence of thermal activation.

6

For operating regimes in which relaxation phenomena or magnetic after-effects are negligible, the local average magnetization $\overline{M}$ is determined directly through minimization of G. For the Helmholtz relation (2), enforcement of the sufficient condition $\frac{\partial G}{\partial M} = 0$ yields

$$\overline{M}(H) = \frac{\mu_0}{\eta}H + M_R\delta \tag{4}$$

where, again, $\delta = 1$ for positively oriented moments and $\delta = -1$ for those with negative orientation. To quantify δ in terms of initial moment configurations and previous switches, we employ Preisach notation and take

$$[\overline{M}(H; H_c, \xi)](t) = \begin{cases} [\overline{M}(H; H_c, \xi)](0) & , \tau(t) = \emptyset \\ \frac{\mu_0}{\eta}H - M_R & , \tau(t) \neq \emptyset \text{ and } H(\max \tau(t)) = -H_c \\ \frac{\mu_0}{\eta}H + M_R & , \tau(t) \neq \emptyset \text{ and } H(\max \tau(t)) = H_c. \end{cases} \tag{5}$$

Here

$$H_c = \frac{\eta}{\mu_0}(M_R - M_I) \tag{6}$$

denotes the local coercive field and

$$\tau(t) = \{t_s \in (0, t] \,|\, H(t_s) = -H_c \text{ or } H(t_s) = H_c\}$$

denotes transition times. The initial moment orientation is given by

$$[\overline{M}(H; H_c, \xi)](0) = \begin{cases} \frac{\mu_0}{\eta}H - M_R & , H(0) \leq -H_c \\ \xi & , -H_c < H(0) < H_c \\ \frac{\mu_0}{\eta}H + M_R & , H(0) \geq H_c. \end{cases}$$

The behavior of $\overline{M}$ given by (4) or (5) is depicted in Figure 5(b) and Figure 6(b).

We note that enforcement of $\frac{\partial G}{\partial M} = 0$ with ψ given by (1) yields the familiar Ising relation

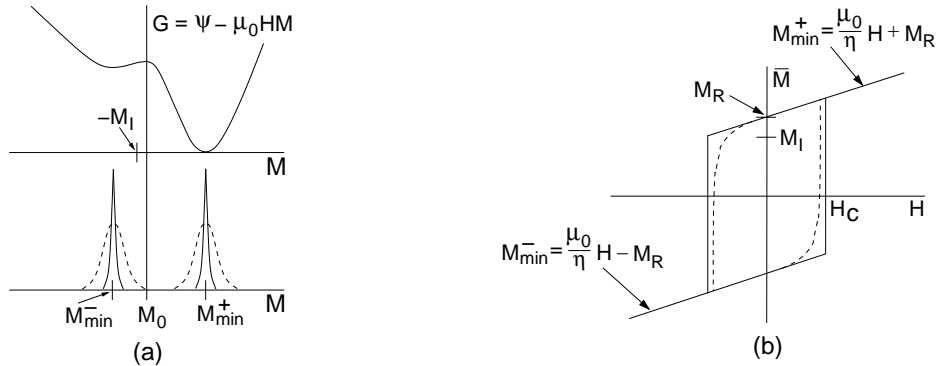$$\overline{M}(H) = M_s \tanh\left(\frac{H + \alpha M}{a(T)}\right) \tag{7}$$

Figure 6: (a) Gibbs energy profile with a high level $(---)$ and low level (———) of thermal activation in the Boltzmann probability $\mu(G) = Ce^{-GV/kT}$. (b) Local magnetization $\overline{M}$ given by equation (9) with high thermal activation $(---)$ and limiting magnetization $\overline{M}$ specified by (4) or (5) in the absence of thermal activation (———).

where $\alpha = \frac{H_h}{\mu_0 M_s}$ and $a(T) = \frac{H_h T}{\mu_0 T_c}$. The incorporation of the magnetization M in the effective field $H_e = H + \alpha M$ guarantees that hysterons specified by (7) exhibit noncongruency as measured for certain materials or operating regimes — e.g., Stoner–Wohlfarth particles.

For regimes in which thermal relaxation or magnetic after-effects are significant, the Gibbs energy and relative thermal energy kT/V are balanced through the Boltzmann relation

$$\mu(G) = Ce^{-GV/kT} \tag{8}$$

which quantifies the probability of obtaining the energy level G — see Section 2.6.2 of [24] for an energy derivation of (8). Here k, V and C respectively denote Boltzmann's constant, a reference volume, and an integration constant chosen to ensure integration to unity.

The local average magnetization expression which incorporates thermal relaxation is

$$\overline{M} = x_+ \langle M_+ \rangle + x_- \langle M_- \rangle \tag{9}$$

where x_+ and x_- respectively denote the fractions of moments having positive and negative orientations and $\langle M_+ \rangle, \langle M_- \rangle$ are the associated average magnetizations. The latter are quantified by the general relations

$$\langle M_+ \rangle = \int_{M_I}^{\infty} M\mu(G)\, dM \quad , \quad \langle M_- \rangle = \int_{-\infty}^{-M_I} M\mu(G)\, dM$$

which, upon evaluation of the integration constant, yields

$$\langle M_+ \rangle = \frac{\displaystyle\int_{M_I}^{\infty} Me^{-G(H,M)V/kT}dM}{\displaystyle\int_{M_I}^{\infty} e^{-G(H,M)V/kT}dM} \quad , \quad \langle M_- \rangle = \frac{\displaystyle\int_{-\infty}^{-M_I} Me^{-G(H,M)V/kT}dM}{\displaystyle\int_{-\infty}^{-M_I} e^{-G(H,M)V/kT}dM}. \tag{10}$$

The evolution of moment fractions are quantified by the differential equations

$$\begin{aligned} \dot{x}_+ &= -p_{+-}x_+ + p_{-+}x_- \\ \dot{x}_- &= -p_{-+}x_- + p_{+-}x_+ \end{aligned} \tag{11}$$

which can be simplified to

$$\dot{x}_+ = -p_{+-}x_+ + p_{-+}(1 - x_+)$$

through the identity $x_+ + x_- = 1$. Here

$$p_{+-} = \frac{1}{\mathcal{T}}\frac{\displaystyle\int_{M_I-\epsilon}^{M_I} e^{-G(H,M)V/kT}dM}{\displaystyle\int_{M_I-\epsilon}^{\infty} e^{-G(H,M)V/kT}dM} \quad , \quad p_{-+} = \frac{1}{\mathcal{T}}\frac{\displaystyle\int_{-M_I}^{-M_I+\epsilon} e^{-G(H,M)V/kT}dM}{\displaystyle\int_{-\infty}^{-M_I+\epsilon} e^{-G(H,M)V/kT}dM} \tag{12}$$

respectively denote the likelihoods that moments switch from positive to negative, and conversely. In these relations, ϵ is a small positive constant and $\mathcal{T}$ denotes the material-dependent relaxation time so that $\omega = \frac{1}{\mathcal{T}}$ quantifies the frequency at which moments attempt to switch.

As depicted in Figure 6, the local magnetization relation (9) incorporates moment switching due to thermal processes in advance of fields required to eliminate minima of G. This mollifies the switching profile and reduces the local coercive field as compared with the thermally inactive hysteron (4) or (5). It is proven in [24, 25] that the thermally active magnetization relation (9) converges to the relation (7) in the limit $kT/V \to 0$ of negligible relative thermal energy.

8

To incorporate the effects of polycrystallinity, material and field nonhomogeneities, inclusions, and texture, we make the assumption that lattice nonhomogeneities produce a distribution of Gibbs energy relations of the form (3). This variability can be incorporated through the assumption that the local coercive field H_c given by (6) and interaction field H_I are stochastically distributed with respective unnormalized densities ν_1 and ν_2 which satisfy the decay criteria

$$
\begin{aligned}
&\text{(i)} \quad \nu_1(x) \ \text{ defined for } \ x > 0, \\
&\text{(ii)} \quad \nu_2(-x) = \nu_2(x), \\
&\text{(iii)} \quad |\nu_1(x)| \le c_1 e^{-a_1 x} \quad , \quad |\nu_2(x)| \le c_2 e^{-a_2|x|}
\end{aligned}
\tag{13}
$$

for positive c_1, a_1, c_2, a_2. These assumptions enforce the physical properties that local coercive fields are positive, low-field Rayleigh loops are symmetric [2], and local coercive and interaction fields decay as a function of distance. As detailed in [24–26], one choice for ν_1 and ν_2 which facilitates implementation and provides sufficient accuracy for various materials and applications is

$$
\begin{aligned}
\nu_1(H_c) &= \frac{c_1}{I_1} e^{-[\ln(H_c/\overline{H}_c)/2c]^2} \\
\nu_2(H_I) &= c_2 e^{-H_I^2/2b^2}
\end{aligned}
\tag{14}
$$

where c_1, c_2, b are positive constants and $I_1 = \int_0^\infty \nu_1(H_c)dH_c$; if the densities are normalized, we note that $I_1 = 1$. It is shown in [15] that the mean and variance of the lognormal distribution satisfy the properties

$$
\langle H_c \rangle \approx \overline{H}_c \quad , \quad \sigma \approx 2\overline{H}_c c
\tag{15}
$$

if $\overline{H}_c$ is large compared with c.

The resulting macroscopic magnetization model is

$$
M(H) = \int_0^\infty \int_{-\infty}^\infty \nu_1(H_c)\nu_2(H_I)\overline{M}(H + H_I; H_c, \xi)] \, dH_I \, dH_c
\tag{16}
$$

with $\overline{M}$ given by (4), (5) or (9). Approximation of the integrals in (16) yields

$$
M(H) = \sum_{i=1}^{N_i} \sum_{j=1}^{N_j} \nu_1(H_{c_i})\nu_2(H_{I_j})\overline{M}(H_{I_j} + H; H_{c_i}, \xi_j) v_i w_j
\tag{17}
$$

where H_{I_j}, H_{c_i} are abscissas and v_i, w_j are quadrature weights.

Because local coercive fields play no role in the anhysteretic material behavior, the global anhysteretic model is

$$
M_{an}(H) = \int_0^\infty \nu_2(H_I)\overline{M}_{an}(H + H_I)dH_I.
\tag{18}
$$

For thermally inactive regimes, the kernel is given by

$$
\begin{aligned}
\overline{M}_{an}(H + H_I) &= \frac{\mu_0}{\eta}(H + H_I) + M_r\delta(H; H_I) \\
\delta(H; H_I) &= \text{sign}(H + H_I)
\end{aligned}
\tag{19}
$$

whereas one would employ the kernel (9) to incorporate magnetic after-effects.

Details regarding the construction, implementation, and accuracy of these models for various ferromagnetic materials can be found in [24–26].

Remark 1 *In the magnetomechanical model developed in Section 3, the stress-induced decay in the coercive field, shown in Figure 4, is incorporated by positing a phenomenological expression for the mean $\overline{H}_c(\sigma, \frac{d\sigma}{dt})$ in (14) which depends on σ and $\frac{d\sigma}{dt}$.*

Remark 2 *The stress-dependent interaction field variance exhibited by the data plotted in Figure 1 is incorporated in the model developed in Section 3 through the introduction of a stress-dependent variance $b^2(\sigma)$ of the normal density ν_2.*

3   Magnetomechanical Model

To incorporate the magnetomechanical effects detailed in Section 1 and illustrated in Figures 1–4, we consider three extensions to the hysteresis framework outlined in Section 2: (i) formulation of a more general Gibbs energy relations which incorporates the elastic energy and effects of magnetomechanical coupling, (ii) development of a stress-dependent expression for the mean $\overline{H}_c(\sigma)$ employed in the relation (14) for the coercive field density, and (iii) development of a stress-dependent relation for the variance $b^2(\sigma)$ of the interaction field density $\nu_2(H_I)$ employed in the hysteresis model (16) and anhysteretic model (18). We note that in the absence of stresses or instance of negligible applied stresses, the magnetomechanical model reduces to the ferromagnetic hysteresis framework summarized in Section 2.

3.1   Gibbs Energy

We consider material characterization and actuator and sensor designs for which applied fields and stresses are co-axial which permits the use of scalar magnetization and strain relations. To incorporate the stress-dependent anhysteretic behavior shown in Figure 2, we extend the Gibbs relation (3) to

$$G(H, M, \sigma, \varepsilon) = \psi(M) + \gamma_4 M^4 + \frac{1}{2} Y^M \varepsilon^2 - \gamma_1(\sigma) Y^M \varepsilon M^2 - \gamma_2(\sigma) Y^M \varepsilon M^4 - \mu_0 H M - \sigma \varepsilon \quad (20)$$

where ψ is given by (2). Here Y^M denotes the Young's modulus at constant magnetization, ε is the uniaxial strain, $\gamma_1(\sigma)$ and $\gamma_2(\sigma)$ are stress-dependent magnetoelastic coupling coefficients, and γ_4 is a constant magnetoelastic coefficient.

For a fixed magnetization level, enforcement of the sufficient condition $\frac{\partial G}{\partial \varepsilon} = 0$ yields the nonlinear constitutive relation

$$\sigma = Y^M \varepsilon - Y^M \lambda(\sigma) \quad (21)$$

where

$$\lambda(\sigma) = \gamma_1(\sigma) M^2 + \gamma_2(\sigma) M^4 \quad (22)$$

denotes the stress-dependent magnetostriction. Following the approach in Jiles [17], we employ two-term Taylor expansions

$$\gamma_1(\sigma) = \gamma_1(0) + \sigma \gamma_1'(0)$$
$$\gamma_2(\sigma) = \gamma_2(0) + \sigma \gamma_2'(0) \quad (23)$$

for the coupling coefficients. It should be noted that the anhysteretic curves will not cross if $\gamma_2(\sigma) = 0$ and hence only quadratic magnetoelastic coupling terms are employed in the Gibbs energy. Moreover, if the magnetostriction is independent of stress, and hence $\gamma_1'(0) = \gamma_2'(0) = 0$, the anhysteretic curves will cross at a single point. The anhysteretic behavior shown in Figure 2 dictates the retention of all four components. Additionally, the quartic term $\gamma_4 M^4$ is included to maintain continuity between the

internal energy quantified by the Helmholtz energy and the magnetoelastic energy. The coefficients $\gamma_1(0), \gamma_1'(0), \gamma_2(0), \gamma_2'(0)$ and γ_4 are identified through a least squares fit to the data.

For operating regimes in which thermal excitation is sufficient to cause discernible magnetic after-effects, the local magnetization $\overline{M}$ is specified by (9) with the Gibbs relation (20) employed in (10)–(12). For regimes in which thermal activation is negligible, enforcement of the sufficient condition $\frac{\partial G}{\partial M} = 0$ yields the stress-dependent magnetization relation

$$[4\gamma_4 - 4\gamma_2(\sigma)\sigma]M^3 + [2\gamma_1(\sigma)\sigma - \eta]M + [-\mu_0 H - \delta\eta M_R] = 0. \tag{24}$$

For model construction, this cubic relation can be solved either using a gradient-based optimization method or directly using the cubic formula summarized in Appendix A.

3.2 Stress-Dependence of $\overline{H}_c(\sigma)$

It is illustrated in Figures 2 and 3 that for fixed field inputs, the application of sufficiently large compressive or tensile stresses will drive the magnetization M to the anhysteretic curve M_{an} (equivalently B to B_{an}). As noted in Section 1.3, this can be interpreted as stress-induced elimination of local minima associated with pinning sites and easy axes so that the magnetization achieves the global minimum associated with M_{an}. One manifestation of this phenomenon is that local coercive fields H_c are driven to zero since single-valued anhysteretic curves indicate the absence of H_c.

One mechanism which contributes to this "approach to the anhysteretic" is 90° switching and 90° domain wall movement. As discussed in Section 1.2, however, the measured asymmetry between compressive and tensile stresses prohibits a sole reliance on this mechanism and a complete characterization of energy phenomena contributing to this effect presently precludes the development of macroscopic models that are sufficiently efficient for transducer design and control implementation. Instead, we provide a phenomenological characterization of the coercive field mean $\langle H_c(\sigma)\rangle \approx \overline{H}_c(\sigma)$ which accommodates the phenomena discussed in Sections 1.2 and 1.3.

Consider the representation

$$
\begin{aligned}
\overline{H}_c(\sigma) &= \widehat{H}_c e^{-\left(k_1 + \left|\frac{d\sigma}{dt}\right|\left(\widehat{k}_2\sigma + \widehat{k}_3\sigma^2 + \widehat{k}_4\mathrm{sgn}(\sigma)\right)\sigma\right)\sigma} \\
&= \widehat{H}_c e^{-\left(k_1\sigma + k_2\sigma^2 + k_3\sigma^3 + k_4|\sigma|\right)}
\end{aligned} \tag{25}
$$

where $k_2 = \widehat{k}_2\left|\frac{d\sigma}{dt}\right|$, $k_3 = \widehat{k}_3\left|\frac{d\sigma}{dt}\right|$ and $k_4 = \widehat{k}_4\left|\frac{d\sigma}{dt}\right|$. The fourth term in the exponential incorporates the slope discontinuity discussed in item (ii) of Section 1.2. The second and fourth terms provide symmetry for low compressive or tensile stresses whereas the first and third terms provide asymmetry. For fixed stresses, we note that $k_2 = k_3 = k_4 = 0$. The behavior of $H_c(\sigma)$ with positive k_1, k_2, k_3 and $k_4 = 0, k_4 > 0$ is illustrated in Figure 7.

The relation (25) quantifies the reduction in coercive fields achieved during the application of tensile or compressive stresses but it does not designate the retention of achieved coercive fields when applied stresses are released. To illustrate, consider the Pitman data shown in Figure 4(c). The relation (25) is used to quantify $\overline{H}_c(\sigma)$ as compressive stresses are increased from 0 MPa to -400 MPa but the mean remains at $\overline{H}_c(\sigma) = \overline{H}_c(-400)$ as stresses are returned to 0 MPa. For this complete compressive cycle, the mean coercive field is quantified by the relation

$$
\overline{H}_c(\sigma) = \begin{cases}
\widehat{H}_c e^{-\left(k_1\sigma + k_2\sigma^2 + k_3\sigma^3 + k_4|\sigma|\right)} & , \quad \frac{d\sigma}{dt} < 0 \\
\overline{H}_c(\sigma_{\min}) & , \quad \frac{d\sigma}{dt} > 0
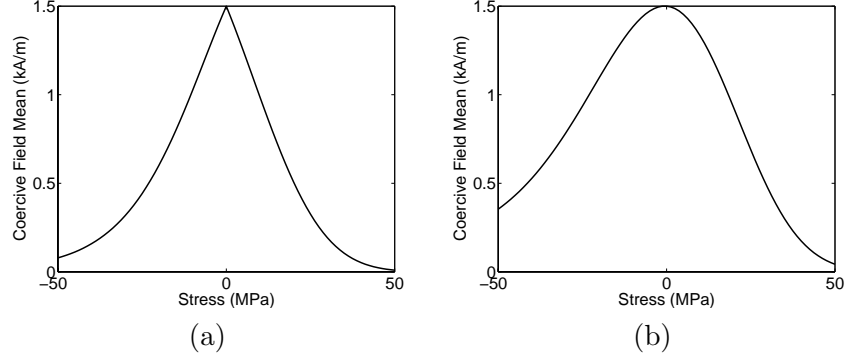\end{cases} \tag{26}
$$

11

Figure 7: Behavior of $\overline{H}_c(\sigma)$ given by (25) with $\widehat{H}_c, k_1, k_2, k_3 > 0$ and (a) $k_4 = 0$, (b) $k_4 > 0$.

where $\sigma_{\min} = -400$ MPa for this example. Similarly, a single tensile cycle would be quantified using the expression

$$\overline{H}_c(\sigma) = \begin{cases} \widehat{H}_c e^{-\left(k_1\sigma + k_2\sigma^2 + k_3\sigma^3 + k_4|\sigma|\right)} & , \quad \frac{d\sigma}{dt} > 0 \\ \overline{H}_c(\sigma_{\max}) & , \quad \frac{d\sigma}{dt} < 0 \,. \end{cases} \tag{27}$$

Analogous relations based on previous minima and maxima can be used to characterize the mean coercive field for multiple cycles.

To construct the density $\nu_1(H_c)$ given by (14) for a specific material, the parameters $\widehat{H}_c, k_1, k_2, k_3$ and k_4 are estimated through a least squares fit to data. As illustrated in Section 4, suitable accuracy can be obtained for certain materials and operating conditions with null values for certain parameters.

Remark 3 *We note that (25)–(27) can be interpreted as parametric representations for an unnormalized density for the local coercive field mean.*

3.3 Stress-Dependence of $b^2(\sigma)$

It is noted in Section 1.1 and illustrated in Figure 1 that applied stresses can significantly alter both the remanence magnetization M_R (or remanence induction B_R) and the differential susceptibility $\frac{dM}{dH}$ or differential permeability $\frac{dB}{dH}$ at remanence. The reduction in M_R and $\frac{dM}{dH}$ for large compressive stresses can be attributed in part to local interaction fields H_I which cause switching in advance of a sign reversal in applied fields H. As detailed in Goodenough [16], local interaction field behavior and associated domains having reversed magnetization are influenced by a number of factors pertaining to domain wall formation including (i) magnetic annealing and cold rolling to reduce misalignment between grains, and (ii) alignment of easy axes for varied grain orientations through the application of tensile stresses. The first mechanisms provide means for controlling the shape of hysteresis loops and reducing the stress-dependence of local interaction fields — e.g., the anhysteretic and hysteresis data reported in [18] and summarized in Figure 2 exhibit minimal stress-dependence in H_I compared with the Pitman data shown in Figure 1.

To characterize stress-dependence in H_I for materials where it is significant, we consider the influence of stress on the density $\nu_2(H_I)$. For large tensile stresses, the dearth of pre-remanence switching indicates a small variance b^2 for H_I and hence the effective field $H_e = H + H_I$ — we assume no variation in the applied field H — as depicted in Figure 8(a). For large compressive stresses, there is significant pre-remanence switching which indicates large b^2 as depicted in Figure 8(b). The variance b^2 thus exhibits the qualitative stress-dependence depicted in Figure 9(a) and 9(b) depending on the degree of emphasis placed on saturating effects for large compressive stresses.
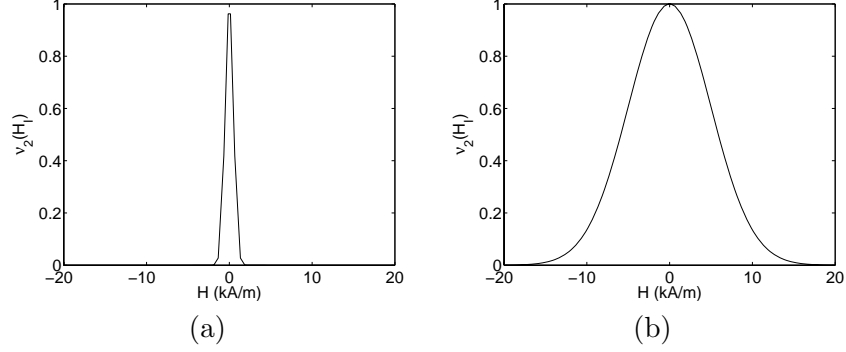
Figure 8: Interaction field density $\nu_2(H_I)$ with (a) small variance b^2, and (b) large variance b^2.

In Section 4.2, we employ a polynomial relation of the form

$$b^2(\sigma) = b_0 + b_1\sigma + b_2\sigma^2 + b_3\sigma^3, \tag{28}$$

which yields the form shown in Figure 9(a), when characterizing the steel data shown in Figure 1. Analogous relations yielding the behavior shown in Figure 9(b) can be employed if dictated by the data. We note that when constructing spline representations of the form (28) for $b^2(\sigma)$, units should be chosen to avoid overflow errors (e.g., MPa rather than Pa).
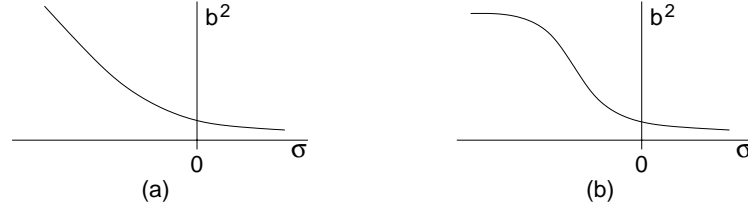

Figure 9: Interaction field variance with (a) saturation at large tensile stresses, and (b) saturation for large tensile and compressive stresses.

3.4 Model Parameters

The units, definitions, and interpretations of parameters employed in the magnetomechanical model are compiled in Table 1.

Parameter	M_R	η	c	$\widehat{H}_c$	$b^2(\sigma)$	$C = c_1 \cdot c_2$	γ_4	
Units	kA/m			kA/m	$\mathrm{A^2 m^{-2}}$		$\mathrm{A^{-4} m^4}$	
Equation	(2)	(2)	(14)	(25)	(14)	(14)	(20)	
Physical	Local	$\frac{dH}{dM}$ after	Variability	Mean of	Variance	Linear	Energy	
Meaning	rem.	switching	of H_c	H_c $(\sigma = 0)$	of H_I	scale	term	
Parameter	$\gamma_1(0)$	$\gamma_1'(0)$	$\gamma_2(0)$	$\gamma_2'(0)$	k_1	k_2	k_3	k_4
Units	$\mathrm{A^{-2} m^2}$	$\mathrm{A^{-2} m^2 Pa^{-1}}$	$\mathrm{A^{-4} m^4}$	$\mathrm{A^{-4} m^4 Pa^{-1}}$	$\mathrm{Pa^{-1}}$	$\mathrm{Pa^{-2}}$	$\mathrm{Pa^{-3}}$	$\mathrm{Pa^{-1}}$
Equation		(20) and (23)				(25)		
Meaning		Energy Coefficients				Coercive Field Coefficients		

Table 1: Parameters to be identified for model construction.

4 Model Validation

To illustrate attributes of the magnetomechanical model, we consider four examples in which it is used to characterize steel and iron data sets from Jiles and Atherton [18], Pitman [21], Birss, Faunce and Isaac [3] and Craik and Wood [10] for a variety of compounds and input conditions. Details regarding the specific materials and experimental conditions can be found in the respective citations. Additional examples illustrating the performance of the model in the absence of applied stresses can be found in [6, 24–26].

4.1 Jiles and Atherton Data

The data reported in [18] was obtained from a steel sample of length 6 cm and cross-sectional area 1 cm. The composition (% by weight) of the sample was C (0.08), Mn (1.98), S (0.08), P (0.015), Cu (0.055) and Mo (0.235).

The anhysteretic model (18) is more fundamental than the hysteresis model (16) in the sense that it does not require local coercive fields. Hence parameters in (18) with the kernel (4) were estimated first through a least squares fit to the anhysteretic data shown in Figure 2 to obtain the values summarized in Table 2. We note that $k_2 = k_3 = k_4 = 0$ since $|\frac{d\sigma}{dt}| = 0$. Because the data exhibits minimal interaction field variability, we employed the constant variance relation $b^2(\sigma) = b_0$ and hence took $b_1 = b_2 = b_3 = 0$ in (28). The resulting model fits, with induction values computed using the relation $B = \mu_0(M + H)$, are shown in Figure 10 where it is observed that through the use of the two-term Taylor expansion (23), the model quantifies the multiple crossing points associated with the Villari effect.

To characterize the hysteresis data plotted in Figure 11, the measured coercive field $\mathcal{H}_c = 0.91$ kA/m was employed as an initial value and the parameters $\overline{H}_c$ and c compiled in Table 2 were estimated through a least squares fit to the symmetric major loop data. Measured periodic fields having lower amplitudes were subsequently input to the model — using the *same* parameter values — to obtain the symmetric minor loop *predictions* which are also plotted in Figure 11. It is observed that the model accurately characterizes the hysteretic material behavior throughout the drive regime, including the approximately quadratic Rayleigh loop behavior at low input fields. The performance of the framework employing the piecewise quadratic Gibbs relation (3) with $\sigma = 0$ is illustrated in [25].

Parameter	M_R	η	c	$\widehat{H}_c$	$b^2(\sigma)$	$C = c_1 \cdot c_2$	γ_4	
[18] Data	5.40	2.77e-6	0.8	0.25	9.5e+6	1.9e-2	6.6e-15	
[21] Data	5.40	1.16e-5	0.1	0.8	see (29)	255.9	8.6e-15	
[3] Data	0.74	2.76e-6	0.4	0.028	2.0e+3	9.0	2.5e-14	
[10] Data	0.45	3.82e-6	0.9	0.015	1.5e+3	13.2	3.95e-11	
Parameter	$\gamma_1(0)$	$\gamma_1'(0)$	$\gamma_2(0)$	$\gamma_2'(0)$	k_1	k_2	k_3	k_4
[18] Data	4.15e-15	-4.0e-25	-4.65e-23	-6.8e-32	1.0e-9	0	0	0
[21] Data	4.11e-15	-4.9e-24	-4.08e-23	-6.8e-22	2.2e-9	2.0e-17	-1.0e-26	1.2e-8
[3] Data	9.5e-14	-9.1e-23	-5.0e-21	-1.0e-27	1.1e-9	1.0e-15	-1.5e-23	1.0e-8
[10] Data	1.0e-9	-3.5e-22	-4.6e-19	-4.0e-27	1.0e-9	1.0e-17	4.0e-24	5.0e-8

Table 2: Parameters employed in the model fits to data from Jiles and Atherton [18], Pitman [21], Birss, Faunce and Isaac [3] and Craik and Wood [10]
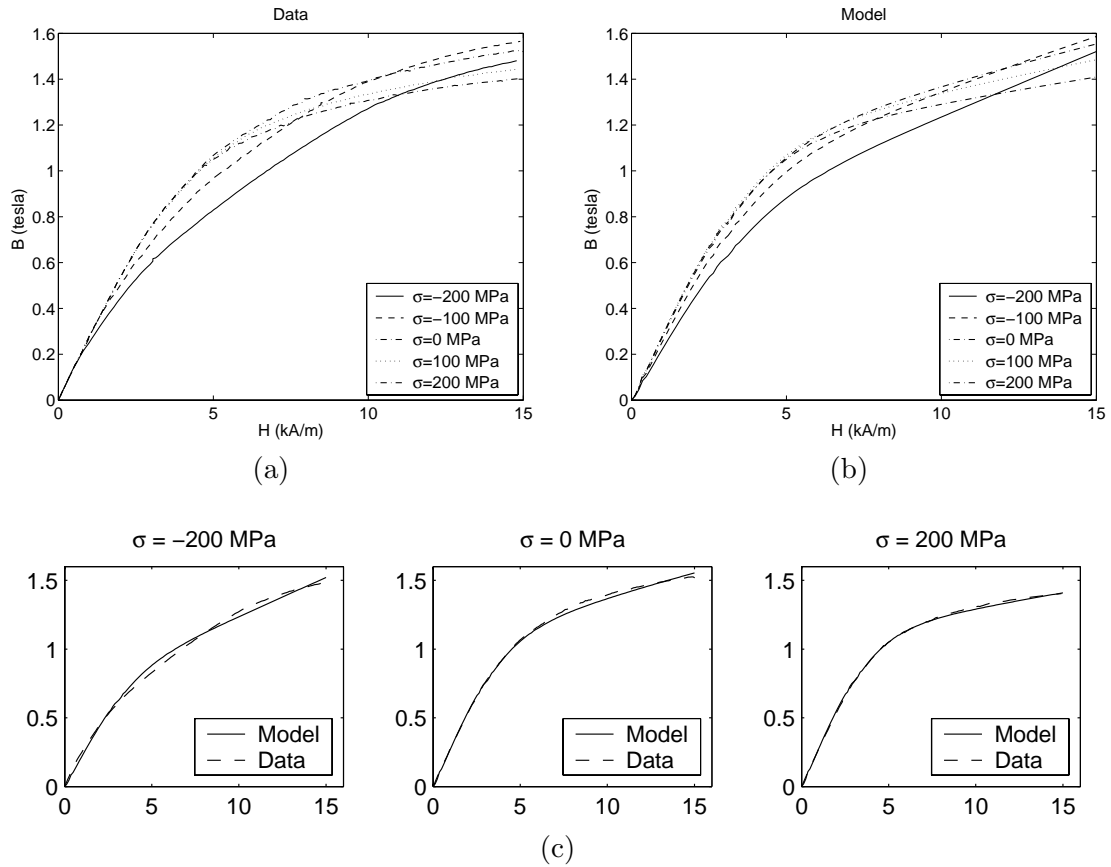
Figure 10: (a) Anhysteretic magnetization data from Jiles and Atherton [18], (b) model fit, and (c) comparison between experimental data and model for stresses of -200 MPa, 0 MPa and 200 MPa. Abscissas: field (kA/m), ordinates: ΔB (tesla).
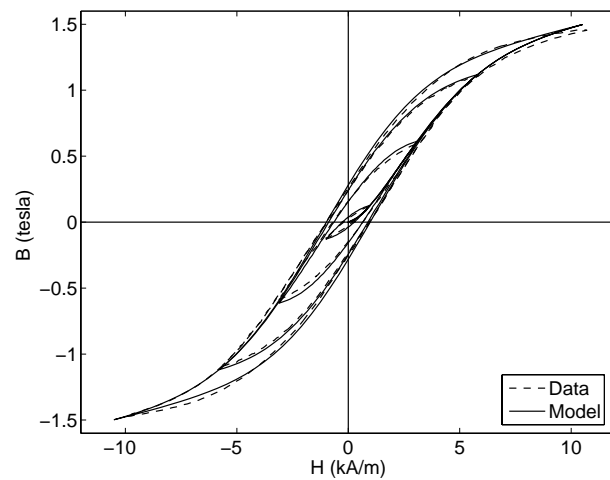

Figure 11: Hysteresis data from Jiles and Atherton [18], major loop fit, and minor loop predictions with $\sigma = 0$.

15

4.2 Pitman Data

The Pitman data plotted in Figures 1 and 4 illustrates two manifestations of the magnetomechanical effect: (i) stress-dependence in the interaction field variance b^2, remanence, and coercive field for certain materials, and (ii) stress-induced approach to the anhysteretic magnetization M_{an} or induction B_{an}.

To estimate the model parameters summerized in Table 1, we first performed a least squares fit to the hysteresis data of Figure 1 which was collected at fixed stresses ranging from 100 MPa to -400 MPa. This yielded the parameter values summarized in Table 2, except for k_2–k_4 which are zero when $\frac{d\sigma}{dt} = 0$, as well as the coefficients

$$b_1 = 1.0 \times 10^5 \ , \ b_2 = -1.4983 \times 10^4 \ , \ b_3 = 1.7075 \times 10^2 \ , \ b_4 = -2.5917 \times 10^{-1} \tag{29}$$

in the variance relation (28). The model fits in Figure 12 illustrate that the framework quantifies the decrease in remanence, increase in coercive field, and decrease in differential permeability $\frac{dB}{dH}$ which occur as compressive stresses of increasing magnitude are applied to the steel rod.

To characterize the decay to the anhysteretic shown in Figure 3, we simulated the experimental conditions described in Section 1.3. The model was drive to positive or negative saturation and then
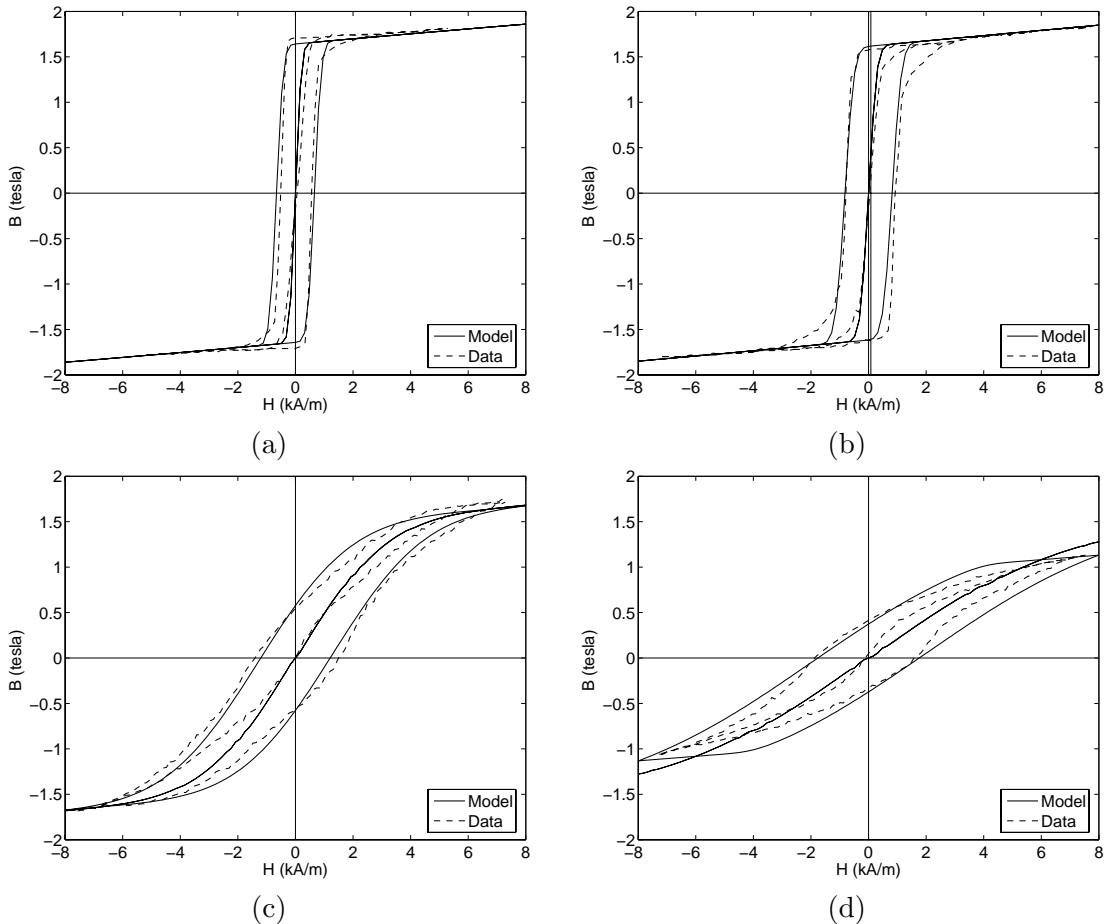

Figure 12: Hysteretic and anhysteretic data from Pitman [21] and model fits for stresses of (a) 100 MPa, (b) 0 MPa, (c) -200 MPa, and (d) -400 MPa. The vertical line at 80 A/m in (b) is the fixed field level for the stress-dependent data and model response in Figure 13.
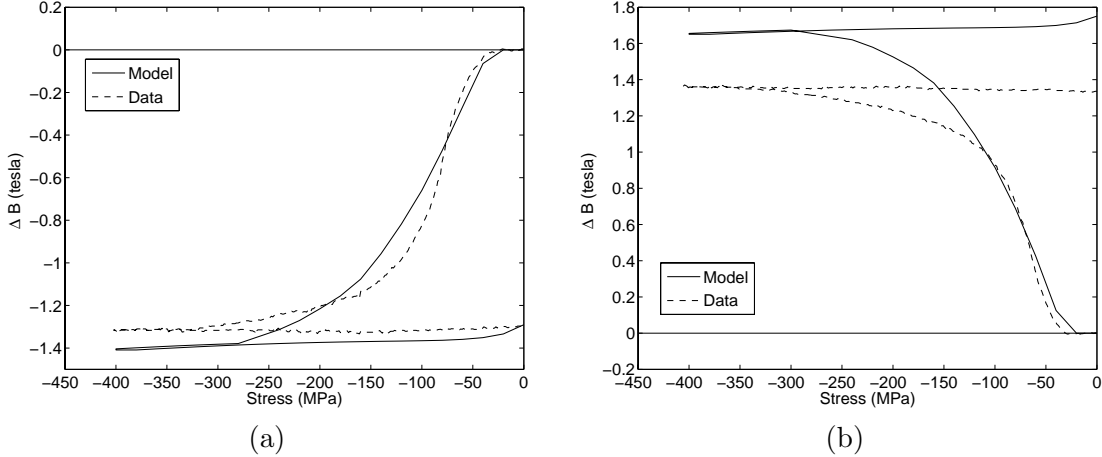
Figure 13: Pitman data [21] and modeled changes in the induction B due to compressive stresses with an initial field of 80 A/m: (a) positive remanence, and (b) negative remanence.

held at the constant field value of 80 A/m, indicated by a vertical line in Figure 12(b), while compressive stresses were applied and subsequently released. Because $\frac{d\sigma}{dt} \neq 0$, this allowed identification of the parameters k_2–k_4 in the relations (25)–(27) used to quantify the local coercive field behavior.

The model fits in Figure 13 demonstrate a reasonably accurate characterization from positive remanence but a modeled prediction of ΔB_{an} which is greater than the experimental value when starting from negative remanence. This is due, at least in part, to a discrepancy in the data. It is observed in the data of Figure 12(b) that the difference between B and B_{an} at 80 A/m is roughly 1.6 tesla whereas the data in Figure 13(b) indicates that the anhysteretic is achieved with ΔB less than 1.4 tesla. A similar, but less significant, discrepancy is noted in the data of Figure 13(a). Hence the modeled behavior in Figure 13 illustrates that the approach to the anhysteretic is consistent with the fixed-stress data in Figure 12.

4.3 Data of Birss, Faunce and Isaac

It was noted in Section 1.2 that tensile and compressive stresses can yield asymmetric changes in B and M, even at low input levels. In this example, we illustrate the performance of the model for characterizing asymmetric induction changes using iron data from Birss, Faunce and Isaac.

As detailed in [3], the spectrographically pure iron specimen had a diameter of 0.3175 cm and length of 9.84 cm so there was negligible bending compression. Furthermore, the sample was annealed at 800 ^{o}C for 1 hour. In the experiments yielding the data shown in Figure 14, the specimen was AC demagnetized at zero stress followed by application of a 40 A/m field. This field value was subsequently held fixed and tensile forces up to 29 MPa were applied and removed. Following AC and stress demagnetization, the same procedure was applied with a tensile force up to 50 MPa. The data for compressive stresses was collected in a similar manner. Analysis of this data indicates that whereas the response is approximately symmetric for low stress inputs, varying degrees of asymmetry are manifested even at pascal-level inputs. The slope reversal at approximately -25 MPa indicates that the anhysteretic induction B_{an} has been reached whereas tensile stresses in excess of 50 MPa are required to drive B to B_{an}.

The model implementation simulated the experimental procedure in the sense that it was initialized at zero magnetization (see [24, 25] for implementation details), a field of 40 A/m was applied and held fixed, and tensile and compressive stresses were applied and removed. A least squares fit to
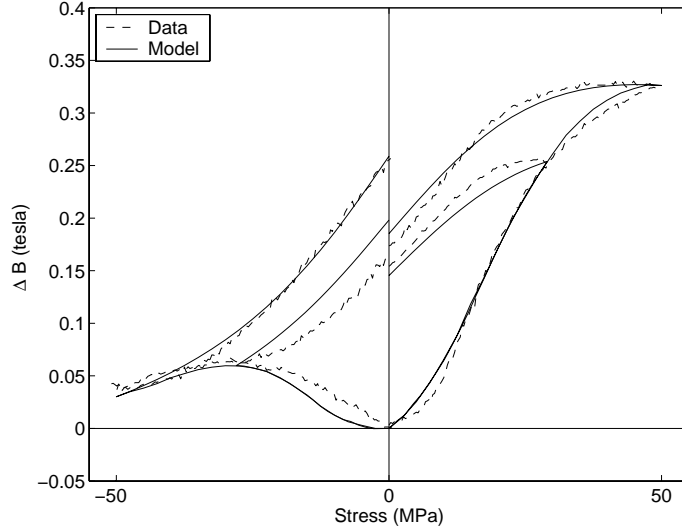
17

Figure 14: Data from Birss, Faunce and Isaac [3] and model predictions for maximum stress inputs of ± 29 MPa and ± 50 MPa at a fixed field value of $H = 40$ A/m.

the data yielded the parameters summarized in Table 2 and model response shown in Figure 14. It is noted that the nonzero values of k_1 and k_3 accommodate the asymmetry noted in the data. Due to the lack of H-B or H-B_{an} data to indicate potential variability in b^2, we employed the constant value $b^2(\sigma) = b_0$. Whereas there is a slight discrepancy between the data and model for low compressive stresses, the framework accurately characterizes the primary magnetomechanical effects manifested in the data.

4.4 Data of Craik and Wood

We illustrate here the performance of the model for characterizing the asymmetric magnetomechanical behavior of mild steel using data reported by Craik and Wood. As detailed in [10], the specimen consisted of a steel strip freely sliding in a slotted yoke to permit application of both tensile and compressive stresses. The experimental procedure is similar to that detailed in Section 4.3, and data collected at fixed field levels of 26.6 A/m, 80 A/m, and 132 A/m with input stresses up to ± 100 MPa is shown in Figure 15(a).

The model fit in Figure 15(b), obtained with the parameter values in Table 2, illustrates that the model characterizes the qualitative material behavior at all three field levels including the reversal in slope when the anhysteretic is reached. The discontinuity in $\frac{dB}{d\sigma}$ at $\sigma = 0$ is accommodated by the k_4 term in the coercive field relations (26)–(27). Hence the model achieves criteria (i) and (ii) of Section 1.2. The primary discrepancy between the model and data occurs after the anhysteretic is achieved where the data exhibits a loss (multivalued loop) upon stress reversal whereas the model predicts no loss. The source of this phenomenon in the data is unexplained and is hypothesized to be due to mechanical losses in the supporting yoke which are not accommodated by the magnetomechanical model.
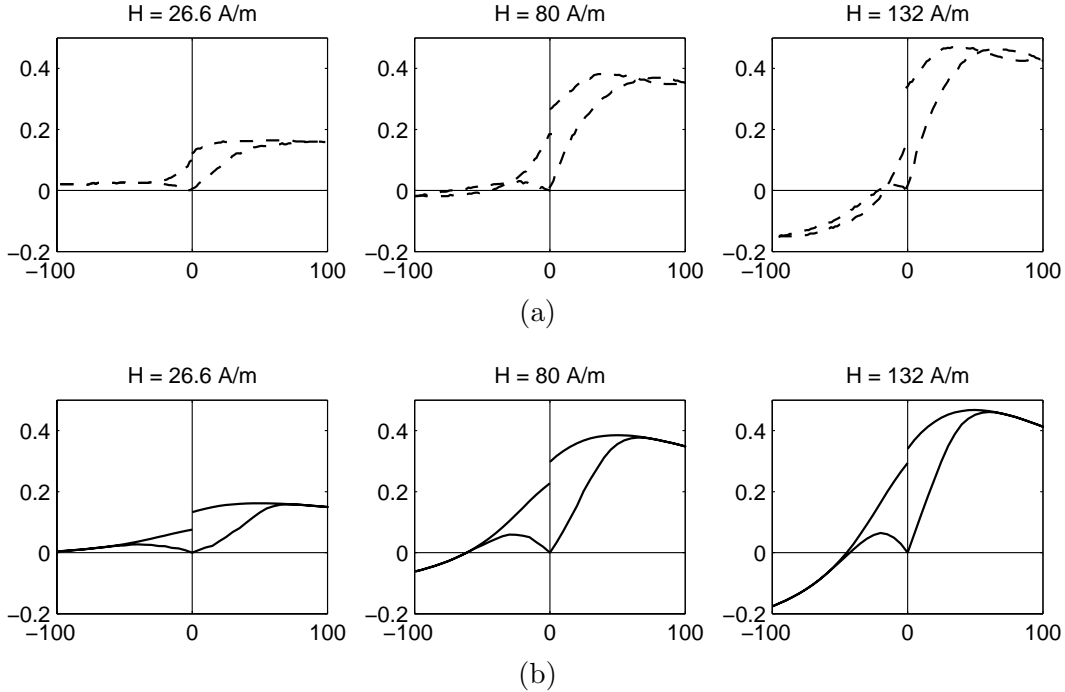
18

Figure 15: (a) Data from Craik and Wood [10], and (b) model fits for 100 MPa inputs at fixed field levels of $H = 26.6$ A/m, $H = 80$ A/m, and $H = 132$ A/m. Abscissas: stress (MPa), ordinates: ΔB (tesla).

5   Concluding Remarks

The model developed in this paper quantifies aspects of the direct magnetomechanical effect inherent to ferromagnetic materials. The nucleus of the model is the framework developed in [24–26] to quantify the hysteretic and nonlinear H-B and H-M behavior of the materials in the absence of applied stresses. In the first step of the development, Helmholtz and Gibbs energy relations are constructed to quantify the internal and magnetostatic energies. For homogeneous and isotropic materials, minimization of the Gibbs energy provides a macroscopic model for operating regimes in which thermal relaxation is negligible. To accommodate thermal relaxation or magnetic after-effects, the Gibbs and relative thermal energies are balanced using Boltzmann principles. In the second step of the development, the effects of polycrystallinity, material nonhomogeneities and inclusions, and variable effective fields are incorporated through the assumption that local coercive and effective fields are manifestations of underlying distributions. Stochastic homogenization in this manner yields low-order models that are sufficiently accurate for a wide range of material characterization and sufficiently efficient to be employed for transducer design and model-based control implementation. It is demonstrated in [6, 24–26] that the original ferromagnetic hysteresis framework accurately quantifies major and biased minor loop behavior, certain accommodation phenomena, and magnetic after-effects in the absence of applied stresses.

The complexity of mechanisms which contribute to the magnetomechanical effect presently precludes construction of low-order macroscopic models based solely on energy principles. To achieve the efficiency required for design and control purposes, we instead use physical principles to motivate phenomenological representations quantifying the effect of stress on the local coercive field mean and interaction field variance. Because the coercive field relation can be interpreted as a paramet-

19

ric representation for an unnormalized density, this approach is commensurate with the strategy underlying both the energy-based hysteresis framework [24–26] and various classical and extended Preisach models of employing stochastic homogenization techniques to improve model accuracy and efficiency when quantifying stochastic, highly complex, or poorly understood physical phenomena. As illustrated through comparison and prediction of experimental data, the resulting model provides the capability for quantifying stress-dependence in the remanence, coercive field, and interaction field variance, the approach to the anhysteretic, and asymmetric tensile/compressive behavior.

The present model was framed in the context of the *a priori* choices (14) of a lognormal representation for the local coercive field and a normal or Gaussian representation for the local interaction field. These choices satisfy the physical requirements (13) but can yield limited accuracy for high fidelity characterization for certain materials and operating conditions. It is demonstrated in [6,24,25] that the identification of general density values $\nu_1(H_{c_i})$ and $\nu_2(H_{I_j})$ provides the framework with additional accuracy and flexibility. The extension of these techniques to magnetomechanical phenomena and the development of techniques to identify general density representations for $\overline{H}_c(\sigma)$ and $b^2(\sigma)$ are under current investigation.

The present framework does not incorporate eddy current losses and hence it should be restricted to drive regimes or transducer designs where these effects are minimal. It also does not incorporate crystalline anisotropy and extension of the theory to accommodate uniaxial and cubic anisotropies constitutes current research. Aspects of the converse magnetomechanical effect have been addressed in [24,26] but comprehensive validation of constitutive relations and transducer models incorporating the combined direct and converse effects is under investigation.

A   Solution of Cubic Equations

Consider the cubic equation

$$z^3 + a_2 z^2 + a_1 z = 0. \tag{30}$$

If we let

$$
\begin{aligned}
q &= \frac{1}{3}a_1 - \frac{1}{9}a_2^2 \\
r &= \frac{1}{6}(a_1 a_2 - 3a_0) - \frac{1}{27}a_2^3,
\end{aligned}
\tag{31}
$$

then the following solution criteria hold:

$$
\begin{aligned}
q^3 + r^2 &> 0, & &\text{one real root, a pair of complex conjugate roots,} \\
q^3 + r^2 &= 0, & &\text{all roots real, at least two are equal,} \\
q^3 + r^2 &< 0, & &\text{all roots real, irreducible case.}
\end{aligned}
$$

The roots are given by

$$
\begin{aligned}
z_1 &= (s_1 + s_2) - \frac{a_2}{3} \\
z_2 &= -\frac{1}{2}(s_1 + s_2) - \frac{a_2}{3} + \frac{i\sqrt{3}}{2}(s_1 - s_2) \\
z_2 &= -\frac{1}{2}(s_1 + s_2) - \frac{a_2}{3} - \frac{i\sqrt{3}}{2}(s_1 - s_2)
\end{aligned}
\tag{32}
$$

where

$$s_1 = \left(r + \sqrt{q^3 + r^2}\right)^{1/3} \quad , \quad s_2 = \left(r - \sqrt{q^3 + r^2}\right)^{1/3}. \tag{33}$$

For the cubic equation (24), q and r are given by

$$q = \frac{1}{12}\left[\frac{\eta - 2\gamma_1(\sigma)\sigma}{\gamma_4 - \gamma_2(\sigma)\sigma}\right] \quad , \quad r = -\frac{1}{8}\left[\frac{\mu_0 H + \eta\delta M_R}{\gamma_2(\sigma)\sigma - \gamma_4}\right].$$

For the parameter choices employed in the validation in Section 4, $q^3 + r^2 > 0$ so we use the real root $z_1 = s_1 + s_2$.

Acknowledgements

References

Note: Center for Research in Scientific Computation Technical Reports can be accessed at the web site http://www.ncsu.edu/crsc/reports.html.

[1] D.L. Atherton and V. Ton, "The effects of stress on a ferromagnet on a minor hysteresis loop," *IEEE Transactions on Magnetics*, 26, pp. 1153–1156, 1990.

[2] G. Bertotti, *Hysteresis in Magnetism: For Physicists, Materials Scientists, and Engineers*, Academic Press, San Diego, CA, 1998.

[3] R.R. Birss, C.A. Faunce and E.D. Isaac, "Magnetomechanical effects in iron and iron-carbon alloys," *Journal of Applied Physics D: Applied Physics*, 4, pp. 1040–1048, 1971.

[4] R.M. Bozorth, *Ferromagnetism*, D. Van Nostrand Company, Inc., New York, 1951.

[5] F. Brailsford, *Magnetic Materials*, Methuen/Wiley, London/New York, 1960.

[6] T.R. Braun, R.C. Smith and M.J. Dapino, "Validation of a homogenized energy model for magnetic after-effects," CRSC Technical Report CRSC-TR05-26; *Applied Physics Letters*, submitted.

[7] W.F. Brown, "Irreversible magnetic effects of stress," *Physical Review*, 75(1), pp. 147–154, 1949.

[8] F.T. Calkins, *Design, Analysis and Modeling of Giant Magnetostrictive Transducers*, PhD Dissertation, Iowa State University, 1997.

[9] S. Chikazumi, *Physics of Ferromagnetism*, 2nd Ed., Carendon Press, Oxford, 1997.

[10] D.J. Craik and M.J. Wood, "Magnetization changes induced by stress in a constant applied field," *Journal of Applied Physics D: Applied Physics*, 3, pp. 1009–1016, 1970.

[11] B.D. Cullity, *Introduction to Magnetic Materials*, Addison-Wesley, Reading, MA, 1972.

[12] M.J. Dapino, "Magnetostrictive materials," *Encyclopedia of Smart Materials*, M. Schwartz, Ed., John Wiley and Sons, New York, pp. 600–620, 2002.

[13] M.J. Dapino, "On magnetostrictive materials and their use in adaptive structures," *International Journal of Structural Engineering and Mechanics,* 17(3-4), pp. 303–329, 2004.

[14] M.J. Dapino, F.T. Calkins and A.B. Flatau, "Magnetostrictive devices," *Wiley Encyclopedia of Electrical and Electronics Engineering*, John G. Webster, Ed., John Wiley and Sons, Inc., New York, Volume 12, pp. 278–305, 1999.

[15] E. Della Torre, *Magnetic Hysteresis*, IEEE Press, New York, 1999.

[16] J.B. Goodenough, "Summary of losses in magnetic materials," *IEEE Transactions on Magnetics*, 38(5), pp. 3398–3408, 2002.

[17] D.C. Jiles, "Theory of the magnetomechanical effect," *Journal of Physics D: Applied Physics*, 28, pp. 1537–1546, 1995.

[18] D.C. Jiles and D.L. Atherton, "Theory of the magnetisation process in ferromagnetics and its application to the magnetomechanical effect," *Journal of Physics D: Applied Physics*, 17, pp. 1265–1281, 1984.

[19] D.C. Jiles and D.L. Atherton, "Theory of ferromagnetic hysteresis," *Journal of Magnetism and Magnetic Materials*, 61, pp. 48–60, 1986.

[20] D.C. Jiles and L.Li, "A new approach to modeling the magnetomechanical effect," *Journal of Applied Physics*, 95(11), pp. 7058–7060, 2004.

[21] K.C. Pitman, "The influence of stress on ferromagnetic hysteresis," *IEEE Transactions on Magnetics*, 26(5), pp. 1978–1980, 1990.

[22] J.B. Restorff, "Magnetostrictive materials and devices," *Encyclopedia of Applied Physics*, Volume 9, pp. 229–244, 1994.

[23] I.M. Robertson, "A review of investigations of the magnetization of steel due to the application of stress," *Materials Forum*, 15, pp. 117–131, 1991.

[24] R.C. Smith, *Smart Material Systems: Model Development*, SIAM, Philadelphia, PA, 2005.

[25] R.C. Smith, M.J. Dapino, T.R. Braun and A.P. Mortensen, "A homogenized energy framework for ferromagnetic hysteresis," CRSC Technical Report CRSC-TR05-08; *IEEE Transactions on Magnetics*, submitted.

[26] R.C. Smith, M.J. Dapino and S. Seelecke, "A free energy model for hysteresis in magnetostrictive transducers," *Journal of Applied Physics*, 93(1), pp. 458–466, 2003.